Haberland, C., Agnon, A., El-Kelani, R., Maercklin, N., Qabbani, I., Rümpker, G., Ryberg, T., Scherbaum, F., Weber, M. (2003): Modeling of seismic guided waves at the Dead Sea Transform. - Journal of Geophysical Research, 108, B7, 2342

DOI: 10.1029/2002JB002309

Modelling of seismic guided waves at the Dead Sea Transform

Christian Haberland[1], Amotz Agnon[2], Radwan El-Kelani[3], Nils Maercklin[1], Issam Qabbani[4], Georg Rümpker[1], Trond Ryberg[1], Frank Scherbaum[5], and Michael Weber[1]

Short title: GUIDED WAVES AT THE DEAD SEA TRANSFORM

[1]GeoForschungsZentrum Potsdam, Germany

[2]Hebrew University, Jerusalem, Israel

[3]An-Najah National University, Nablus, Palestine Territories

[4]Natural Resources Authority, Amman, Jordan

[5]Institute of Geosciences, University Potsdam, Germany

Abstract.

On several recordings of linear seismometer arrays crossing the Arava Fault (AF) in the Middle East, we see prominent wave trains emerging from in-fault explosions which we interpret as waves being guided by a fault-zone related low-velocity layer. The AF is located in the Arava Valley and is considered the principal active fault of the mainly N-S striking Dead Sea Transform System in this section. Observations of these wave trains are confined to certain segments of the receiver lines and occur only for particular shot locations. They exhibit large amplitudes and are almost monochromatic. We model them by a 2D analytical solution for the scalar wavefield in models with a vertical waveguide embedded in 2 quarter spaces. A hybrid search scheme combining genetic algorithm and a local random search is employed to explore the multimodal parameter space. Resolution is investigated by synthetic tests. The observations are adequately fit by models with a narrow, only 3 to 12 m wide waveguide with S-wave velocity reduced by 10 to 60% of the surrounding rock. We relate this vertical low-velocity layer with the damage zone of the AF since the location of receivers observing and of shots generating the guided waves, respectively, match with the surface trace of the fault. The thickness of the damage zone of the AF, at least at shallow depths, seems to be much smaller than in other major fault zones. This could be due to less total slip on this fault.

1. Introduction

In the last few years the analysis of trapped seismic waves has become a powerful tool to study the structure of lithospheric shear zones [e.g., *Hough et al.*, 1994; *Li and Leary*, 1990; *Li et al.*, 1998, 1999, 1994; *Malin et al.*, 1996; *Lou et al.*, 1997]. Similar to light being trapped and very efficiently guided by a glass fibre (owing to its higher refractive index), seismic waves caught by a low-velocity layer can travel as characteristic wave trains over long distances. Due to strong velocity contrasts they are frequently observed in coal seams [e.g., *Dresen and Rüter*, 1994], oil-reservoirs [*Chon et al.*, 1996], and also in tectonically dominated settings such as subduction zones (low-velocity oceanic crust descending into the upper mantle [*Fukao et al.*, 1983; *Abers*, 2000]). In lithospheric fault zones, the structural damage zone related to the deformation is considered to form a low-velocity layer in which guided waves can develop.

Because trapped waves propagate in these layers for considerable portions of the propagation path, they contain valuable information on properties of the narrow zones itself, namely geometry (connectivity, width, spatial orientation) and physical properties (velocities and attenuation). Due to the narrowness of the structures on the one hand and the integrative character of seismic traveltimes and attenuation on the other hand, this information is usually not obtained by conventional seismic investigations (seismic tomography, refraction).

The fault zone guided waves (FZGW) studies up to now included the pure identification and geometrical mapping of waveguides, exemplary studies of principal wave propagation in 2D [*Ben-Zion and Aki*, 1990; *Ben-Zion*, 1998] or 3D structures

[*Igel et al.*, 1997; *Li and Vidale*, 1996; *Huang et al.*, 1995; *Igel et al.*, 2001; *Jahnke et al.*, 2002], and the modelling of observed trapped waveforms [e.g. *Li et al.*, 2000]. For the analysis both earthquakes and explosions [*Li et al.*, 1997b, 1998, 1999] are used as sources.

Most quantitative studies attempt to derive subsurface models by waveform or dispersion curve matching of guided wave observations with synthetic data. Many of them search the model space systematically, and some studies quantify the goodness-of-fit of the models and present equivalent models [e.g. *Peng et al.*, 2000]. In order to account for the complex influence of certain parameters on the appearance of guided waves, *Michael and Ben-Zion* [1998b] proposed the use of genetic algorithm (GA) to search the large parameter space. GA is a very robust global search algorithm [e.g. *Goldberg*, 1989] that proved to be useful in waveform fitting [*Sambridge and Drijkoningen*, 1992; *Sen and Stoffa*, 1992; *Lomax and Snieder*, 1995; *Levin and Park*, 1997].

In this study we present data of explosion generated high-frequency guided waves at the Dead Sea Transform (DST), a 1000 km long, prominent shear zone in the Middle East exhibiting a total slip of ∼100 km during the last 20 Myr. The analysis is part of the interdisciplinary research effort DESERT (**De**ad **Se**a **R**ift **T**ransect) in which several geophysical methods (reflection and refraction seismics, gravimetry, magnetics, electromagnetics) together with geological studies and modelling aim to resolve the structure and dynamics of the transform at different scales. Backbone of the study of the small-scale fault structure was 2D and 3D controlled source high-resolution tomography and reflection seismics. In order to derive subsurface models that best explain the

observations, we model the guided waves by an analytical solution [*Ben-Zion and Aki*, 1990] and search the model space using a hybrid scheme combining GA and a local random search.

2. Geological setting

The SSW-NNE striking DST separates the Arabian plate from the Sinai microplate (see Figure 1). It stretches for approximately 1000 km from the Red Sea Rift to the Taurus-Zagros collision zone. Formed in the Miocene and related to the brake up of the Afro-Arabian continent it accommodates the lateral movement between the two plates. The total amount of left-lateral displacement is $\sim$100 km, recent relative motion is between 3 and 4 mm yr^{-1} [*Klinger et al.*, 2000].

Figure 1.

Between the Gulf of Aqaba/Eilat and the Dead Sea, the sinistral strike-slip Arava Fault (AF) constitutes the major branch of the DST [*Atallah*, 1992; *Garfunkel et al.*, 1981], taking most of the slip. In the central Arava Valley the (straight) fault trace (striking 15 - 20°E) is outlined by scarps, pressure ridges, small rhomb grabens, and water holes. Recent activity is indicated by offset gullies and alluvial fans [*Klinger et al.*, 2000]. Four strong historic earthquakes reportedly hit the AF: 1068 A.D., 1212 A.D., 1293 A.D., and 1458 A.D. [*Ambraseys et al.*, 1994; *Amit et al.*, 2002; *Klinger et al.*, 2000]. These events were corroborated in sedimentary records [*Ken-Tor et al.*, 2001]. By contrast, the current seismic activity along the southern section of the DST is rather small [*Salamon et al.*, 1996]. The region east of the AF is segmented into numerous blocks by additional (W-E and NW-SE striking) faults (some of them normal faults). In the study area, Neogene marl, Cretaceous limestone, and Miocene conglomerates (in the north

Precambrian granite outcrops) are in part covered by young alluvium and aeolian sands.

3. Data and observations

In a specifically designed controlled source experiment we deployed 5 seismic lines crossing the AF at about 30°30'N (see Figure 1). The roughly west-east striking lines 1, 2 and 3, which were approximately 5 km apart, had lengths of about 9 km. Spacing between the 4.5 Hz geophone groups (SM-6, vertical component) on lines 1, 2, and 3 was 100 m. On these long lines signals were recorded by a SUMMIT datalogger (line 1, 250 samples per second) and PDAS-100 dataloggers (lines 2 and 3, 200 Hz per second). Lines 4 and 5 were shorter (ca. 200 m) and had receiver spacings of 10 m. They were equipped with REFTEK dataloggers running with 200 samples per second and with Mark L4-C-3D 1 Hz three component seismometers [*DESERT Team*, 2000; *Maercklin et al.*, 2000].

The fault trace is clearly visible in satellite images over long portions, and it is feasible to identify it in the field at certain segments with an accuracy of better than 100 m. However, to enhance the probability of hitting the fault (and to generate guided waves) we placed 4 groups of 3 individual shots each at locations where we had indications of the fault trace from geological setting, satellite images, or topography. Distance between shots within a group was between 20 and 50 m. At each shotpoint 45 kg of chemical explosives were detonated in 20 m deep boreholes. Due to the use of differential GPS, all positions and heights of shots and receivers could be determined with an accuracy of $\sim$1 m.

We observe prominent high-amplitude, high-frequency wave trains on receiver lines

2, 3, 4, and 5 for two shots, 101 and 102. The observations on line 4 and 5 are shown in Figure 2. They are best developed on line 4 for shots 101 and 102, and on line 5 for shot 101. In general the observations show a series of characteristics, giving evidence of being guided waves. These waves occur only at certain receivers for certain shots. The corresponding receivers are confined to narrow sections of the lines (for positions refer to Figure 1 and Tables 1 and 2). Shots 101 and 102 and the observing receivers on line 4 and line 5 match (within the given accuracy of independent geological information) with the surface trace of the AF. All other shots did not generate such phases. As indicated by bars in Figure 2 the guided waves show very high amplitudes, which are up to 10 times larger than the signals at similar times on other receivers. Offsets between sources and receivers were 2.3 (line 4) and 1.1 km (line 5). Guided waves observed at line 5 show higher frequencies and a shorter duration (ca. 0.2 s instead of 0.3 s) as on line 4, which is expected for shorter offsets.

Table 1.

Table 2.

Figure 2.

Compared to other reported FZGW the guided waves at the AF show rather high frequencies (between 20 and 50 Hz). However, the dominant frequencies are controlled by the geometry and physical properties, and similar high-frequency guided waves are known for example from coal seams [e.g. *Dresen and Rüter*, 1994]. As clearly visible in the time series, the wave trains here are almost monochromatic. Lines 4 and 5 were equipped with 3 component sensors which allowed the determination of the polarization. The phases are vertically polarized, thus only vertical component data is shown in Figure 2. This fact suggests that these phases are Love-type channel waves as described e.g. in *Dresen and Rüter* [1994].

4. Modelling and Inversion

Although influenced by many factors, guided waves are primarily controlled by a 2D structure: a waveguide of 'some' extent with a reduced seismic velocity, and a source within or close to the waveguide. Factors influencing development and shape of guided waves are the amount of velocity reduction within the waveguide, the width of the waveguide, attenuation, and the propagation length. Furthermore, the development of guided waves depends on the position of the seismic source within the waveguide. 3D variations of the 2D waveguide structure, which may concern the waveguide geometry (flexure, branching, bending, interruption, shape, heterogeneities) as well as physical properties of both host rock and wave guide (velocity, gradients), are also known to alter the appearance of guided waves [*Jahnke et al.*, 2002; *Li and Vidale*, 1996; *Igel et al.*, 1997, 2001].

In addition to pure mapping of the waveguide we intend to derive quantitatively some of the model-describing parameters from the observed waveforms. Accordingly, we calculate synthetic seismograms for various models, compare them with the observed waveforms and infer the most probable model from the best fitting data set. Bearing in mind well-known trade-offs among certain parameters [*Ben-Zion*, 1998] and the limitation of our dataset, we restrict ourselves to 2D models. This allows the estimation of effective parameters averaged over the whole propagation length.

We calculated synthetics with a 2D analytical solution for the propagation of waves generated by a SH line source in a single layer $j = 2$ which is embedded within two quarter spaces $j = 1$ and $j = 3$ [*Ben-Zion and Aki*, 1990; *Ben-Zion*, 1998]. The

models are defined by the width of the waveguide w and seismic velocities v_j, seismic attenuation factors $Q_{s,j}^{-1}$ and density ρ of all three layers. Since we intend to model Love-type (shear) guided waves, v_j are shear velocities (i.e., $v_{s,j}$). As in *Ben-Zion* [1998] attenuation was incorporated following *Aki and Richards* [1980]. The receiver can be placed anywhere in the model, and the source anywhere within the single layer. The chosen depth of the source is used as a proxy for the overall propagation length. Synthetic velocity seismograms were band-pass filtered (1 or 4.5 to 90 Hz, respectively) according to instrument response and sampling rate.

The goodness-of-fit between observed and synthetic waveforms was estimated by using the weighted mean of the semblance [*Neidell and Taner*, 1971] of windows of 0.4 s containing the prospective guided wave train of each observed and synthetic trace pair (for a given parameter combination). We inverted simultaneously for up to 11 traces of a shot gather. The use of semblance and the inversion for many traces simultaneously consider the distribution of guided wave energy across the waveguide and in the host rock (leaking) as a major attribute of the observations (in addition to the amplitude and frequency behaviour of the waveforms), thus stabilizing the inversion. See Appendix A for details of the applied objective function.

To efficiently search this multimodal parameter space and to derive an acceptable model (or models) we employ a genetic algorithm (GA). Imitating biological evolution, GA is considered a sturdy optimization technique with the potential of finding global extrema and to follow-up multiple maxima [e.g. *Goldberg*, 1989]. It proved very successful in many optimization problems [e.g. *Carroll*, 1996; *Gibson and Charbonneau*, 1998], especially in seismic (waveform) inversion [*Sambridge and Drijkoningen*, 1992;

Sen and Stoffa, 1992; *Lomax and Snieder*, 1995; *Levin and Park*, 1997]. See Appendix B for details of basic GA.

As in other geophysical applications (with noise present) we are interested in (ideally: all) models equally well explaining the data (within a given accuracy), which would allow the specification of valid parameter bounds. Accordingly, we tuned the GA for a broad sampling of the parameter space rather than for fast convergence: we used a large population size of 50, applied niching (by phenotype sharing) [see for example *Goldberg*, 1989] and turned off the forced reproduction of the best model (no elitism). Furthermore, we combined GA and consecutive local random searches around the best individuals of each generation forming a hybrid scheme. The purpose of this phenotype manipulation is two fold: Assuming optima in the objective function stretching over several neighboring parameter bins, there is a good chance of finding better models in the direct vicinity of an already spotted good model. The second benefit concerns the enhanced exploration of regions with large (however, potentially sub-optimal) values of the objective function (i.e. well fitting models). In each generation we test four randomly chosen models (that is 8% of the population) in the vicinity (within a region of 5% of the allowed parameter bounds) of 10% of the best fitting models, subsequently replacing less-fitting individuals with better ones.

5. Resolution

In order to study the performance of the search and to explore the resolution of the obtained models we conducted synthetic tests. Data were generated for the same source and receiver geometry (same station spacing etc.) as in our experiment, and parameter

settings as shown in Table 3. We added random time shifts of at most $\pm$ 0.005 s and random noise (maximum signal-to-noise ratio of 5) to the synthetics, which we then inverted in the same way as the real data. Synthetic time series are shown in Figure 3.

Table 3.

Figure 3.

We inverted for 4 free parameters: waveguide width w, velocity ratio $v_{s,2}/v_{s,1}$, host rock velocities $v_{s,1}$ and $v_{s,3}$ (which we set identical except for a small perturbation to avoid unrealistic symmetry effects in the synthetics) and an overall attenuation factor ($Q_s^{-1} = Q_1^{-1} = Q_2^{-1} = Q_3^{-1}$). The lateral source position was set fix to one interface between waveguide and host rock. Furthermore, the position of the receiver observing the largest guided wave amplitude was fixed to the centre of the waveguide.

Figure 4 A - D shows values of the fitting function (F) of all in the GA run tested models as a function of the four free parameters. In our implementation of GA search we ran 300 generations (approximately 15,000 tested models) until we achieved a satisfactory fit and a broad sampling of the parameter space. As expected, the GA search reveals a suite of models with an acceptable fit ($F > 0.85$). The best tested model reaches $F = 0.89$, which is the same value as the value associated with the original synthetic model (however, it is not the same model). The distribution of acceptable F-values gives estimates on the resolution of the particular parameter. The threshold of acceptable F-values was determined by visual inspection of the fit for some models. Table 3 summarizes these ranges of the individual parameters and the best retrieved model. The parameter of the synthetic input model (black stars in Figure 4 A-E) plot well within these allowed-parameter limits indicating that the synthetic model is well recovered. However, for particular parameters (i.e. $v_{s,2}/v_{s,1}$ or Q_s^{-1}) these limits are rather large suggesting associated low resolution and/or strong trade-offs. Largest semblance values

of individual traces reach $S = 0.96$. **Figure 4.**

An alternative representation of the acceptable models and a crossplot showing all well fitting models as a function of w and $v_{s,2}/v_{s,1}$, unveils a strong trade-off between these two parameters (Figure 4 E and F). The waveforms can be equally well fitted by certain models with narrow waveguides and large velocity contrasts or wider waveguides and smaller velocity contrasts. All other parameter combinations exhibit no such dependencies but rather random scatter in our synthetic test. Independent constraining information on one of these two parameters (for example from independent seismological or geological studies) could drastically reduce ambiguities. It is noteworthy that gentle variations of w imply (petrophysically) significant variations of $v_{s,2}/v_{s,1}$.

In the recovery test presented above we inverted for four free parameters, and several parameters were not considered in the inversion. Further tests with an individual Q_s^{-1} of the waveguide (both in the synthetic model and as a free inversion parameter) showed that this parameter is not resolved (for the general model and observation geometry used in our test). For synthetic models exhibiting an elevated waveguide-Q_s^{-1} (what is for example discussed for damage zones of faults) the GA search found even well fitting models with reduced waveguide-Q_s^{-1}.

Furthermore, the lateral source position x_0 within the waveguide, which generally influences the shape and development of guided waves, was not included in the search. Sources offset from the waveguide interface result in generally less trapped wave energy and produce a characteristic high-frequency phase superposed on the low-frequency guided wave mode [*Ben-Zion*, 1998, Figure 5 (left)]. Since the latter is not observed in the seismograms we skipped this parameter in the inversion, reducing computational

burden and avoiding further ambiguities.

6. Results

Based on the experience with the synthetic dataset, we inverted the observed data for the same 4 parameters. Figures 5 through 7 show the best fitting models that resulted from the GA searches of data from shots 101 and 102 observed along receiver line 4, and from shot 101 observed along receiver line 5. Due to weak signal, data of shot 102 observed on line 5 were not assessed quantitatively.

Figure 5.

Figure 6.

Figure 7.

The best models reach fitting values around $F = 0.75$. However, single traces reach frequently much higher semblance values ($S \sim 0.85$). Table 4 summarizes all derived parameters and permitted parameter limits. The estimate of accuracy was derived from the distribution of all models with F-values larger than 98% of the F-value of the best model. Remarkable is the narrow waveguide width of between 3 and 30 m, which appears to be well resolved. The density plot (Figure 8) shows that most well fitting models (for observations on line 4) are characterized by a 4 to 6 m wide waveguide. Very similar to the synthetic test, we notice a pronounced trade-off between w and $v_{s,2}/v_{s,1}$ (Figures 5 through 7 E). Although less resolved, Q_s is for all measurements larger than 50.

Table 4.

Figure 8.

The results of both shots for line 4 and also between the two lines are very consistent. For shot 102 many good models with a larger $v_{s,1}$ above 1800 m/s are observed. For the observations along line 5 we derive a slightly smaller $v_{s,1}$ which would be in accordance with the smaller source-receiver offset and, in turn, a smaller penetration depth (smaller velocities). It seems that the observations on line 5 are better explained by smaller

velocity contrasts (above 0.6). Nevertheless, we should keep in mind that the observation along line 5 have only poor signal-to-noise ratio. Figure 9 shows the synthetic traces calculated with arbitrary ”best” models overlaid on the observed time series of shots 101 and 102 observed at line 4, and of shot 101 observed at line 5, showing the good agreement between observations and synthetics.

Figure 9.

Our synthetics are calculated for a SH linesource. In order to check the warranty of this assumption we applied an approximate 2D to 3D transformation to the synthetics for some of the inversions by convolving the time series with $1/\sqrt{t}$ with t being the time [*Vidale et al.*, 1985; *Igel et al.*, 2001; *Ben-Zion et al.*, 2002]. However, we note only minor changes in the well fitting models and the estimates of valid parameter ranges.

On line 3 we observed similar high-frequency wavetrains (not shown) for shots 101 and 102 on a rather broad ($\sim 400\ m$) receiver line segment slightly offset from the AF (see Figure 1). These observations are most likely associated with a SW-NE running fault branch. However, we could not model these observations satisfactorily with 2D analytical synthetics. In principal, variations of our simple model geometry such as low-velocity layers on top of a vertical waveguide or widening of the waveguide toward the surface could explain a spatially broader radiation of high-frequency guided wave energy (general studies of these effects are discussed in *Jahnke et al.* [2002], *Igel et al.* [2001], *Igel et al.* [1997], and *Li and Vidale* [1996]). In fact, shallow high resolution tomographic images of the study area revealed a number of superficial low-velocity features associated with sand dunes and marl [*Maercklin et al.*, 2000]. However, the required numerical (3D) modelling of these observations is beyond the scope of the present paper and will be part of future research.

7. Discussion

We interpret the high-energy late arrivals in our seismic recordings as waves that have been trapped in a sub-vertical low-velocity channel associated with the AF. The strongest argument supporting this interpretation is the fact that we observe these waves only at distinct receivers, and that these waves are generated only by certain sources. So we can rule out pure source or receiver site effects as valid explanations. Recently, *Rovelli et al.* [2002] and *Ben-Zion et al.* [2002] reported on shallow low-velocity structures (maybe better referred to as receiver site structures) instead of deep coherent waveguides which can efficiently trap seismic waves.

The fact, that most positions of the sources and receivers generating and observing guided waves, respectively, match with the surface trace of the AF, suggest, that the waveguide is formed by the damage zone of the fault. Studies on exhumed faults discriminate three major entities within the mesoscopic structure of brittle strike-slip faults [e.g. *Chester et al.*, 1993; *Schulz and Evans*, 2000]: the (undeformed) protolith (host-rock), the damage zone, and the fault core. The fault core (centimetres to decimetres thick) with highly deformed rock is the place where most of the slip is accommodated. The damage zone surrounding the core consists of an increased concentration of faults, fissures and veins. Large fault zones might form a complex network of faults of many sizes [*Wallace and Morris*, 1986].

It was possible to model most of the observations quantitatively. The inversion especially of these high-frequency phases is highly non-unique and can only be applied under certain (restrictive) assumptions (see discussion on constraints above). The

uppermost velocity structure (weathering layer etc.) can cause severe distortions of the high frequency waveforms, which cannot be accounted for by our simple 2D models. This holds also for general 3D variations which could bias both our estimates of the best fitting models and of the acceptable ranges. Moreover, we note that the objective function as revealed by the systematic GA search is characterized by many broad and narrow local maxima of similar amplitude and complex shape [see also *Michael and Ben-Zion*, 1998a]. This means that the observed (noisy) data can be almost equally well explained by many different models [see e.g. *Michael and Ben-Zion*, 1998a] thus yielding in part quite large confidence limits of certain parameters. We believe that these ambiguities and limits are strongly dependent on the experiment geometry, predominant frequencies, used frequency band, etc. in relation to the waveguide geometry and properties. Nevertheless, the parameter searches gave a narrow effective waveguide width of about 3 to 30 m (for the observations on line 4). We favour a very narrow waveguide (3 to 12 m) since in the accompanying high-resolution controlled source tomography experiment we found no evidence for a wider subvertical low-velocity structure at shallow depth. Moreover, trapping efficiency is stronger for larger velocity contrasts, and these are, according to the trade-off curves (Figures 5 to 7 E), allowed for narrow waveguides. Finally, the searches of all independent measurements ended up with best models featuring w between 3 and 12 m.

The apparent narrowness of the AF waveguide (and the deduced damage zone width) puts it in marked contrast to other major fault zones, at which the waveguide width had been deduced by FZGW. For example, *Li et al.* [1990] and *Li et al.* [1997a] report widths of waveguides of the San Andreas fault (SAF), California, of between 100

and 170 m. In the North Anatolian Fault System, *Ben-Zion et al.* [2002] derived fault zone widths on the order of 100 m. The low-velocity zone of the Nojima fault, Japan, has width of 30 - 60 m [*Li et al.*, 1998]. In general, the damage zone thickness seems to be proportional to the total slip along a fault [e.g. *Wallace and Morris*, 1986], with a constant of proportionality of between 10^{-1} and 10^{-3} [*Scholz*, 1987].

Although the whole system of the DST experienced $\sim$100 km of cumulative relative movement since the last 20 Myr, there are indications that several sub-parallel faults were active during that time, thus distributing the total movement. *Eyal et al.* [1981] showed that in eastern Sinai the transform splays to numerous parallel strands, some of which had slipped several kilometres and are inactive now. They have estimated that half of the total 100 km are distributed in eastern Sinai. It is conceivable that the remaining 50 km are distributed between the active AF and parallel strands such as Zofar and or Quaira faults. At the surface and in satellite images several sub-parallel lineaments are visible in the study area, and it is possible that we might have imaged only one of several strands. However, due to the given source and receiver spacing covering a large range of scales (meter to kilometre), we rule out the existence of low-frequency guided waves, and, in turn, larger waveguide widths on a larger scale for the study area.

Another reason for a narrow shallow damage zone could lie in the peculiarities of the two geological units at both sides of the studied AF segment. While the deeper part of the eastern block is mainly formed by Precambrian granites and Cretaceous limestones, the western unit (down to a depth of several kilometres) is mainly formed by sediments of the Hazeva formation and Dana conglomerates, which were - in part syn-kinematically - deposited during the Miocene. Also the eastern unit is partly covered by layers of

Hazeva formation strata and younger sediments. However, structural details are still not known to date. Owing to the fact that we sampled the uppermost part of the AF segment by FZGW (corresponding body P waves penetrate to approximately 300 m depth), we might have imaged the superficial damage zone (several hundreds of meters depth) of the AF that experienced - due to younger age of the involved shallow geological units and syn-depositional faulting - a reduced total slip.

The inversion provides values for the effective shallow host rock shear wave velocity of between 1740 and 1850 m/s. They are slightly smaller for the short-offset observation at line 5 (1570 to 1780 m/s). Together with the observed P wave arrival times this yields a realistic v_p/v_s velocity ratio of the shallow rocks of about 1.8. We notice a wide range of possible velocity reduction within the waveguide of about 10 to 60% of the velocity of the host rock. We think that smaller ratios are more realistic, since the trapping efficiency is larger for these values (see also note above). Similar large values were obtained for example in a conventional seismic experiment at the exhumed San Gregorio Fault (California), where breccia and foliated rock form the damage zone [*Gettemy et al.*, 2001]. FZGW analysis at other major strike-slip faults suggested velocity reductions in the order of 25 to 50% relative to the surrounding rock [e.g. *Li et al.*, 1997a, 1994; *Li and Vernon*, 2001]. Accordingly, the reduced velocities could be interpreted by damaged host rock material within the fault zone. Saline waters are present at the surface trace of the AF (isolated waterholes), and we speculate that aqueous fluids are also present at greater depth of the fault zone. These fluids could also contribute to the velocity reduction of the waveguide. Nevertheless, magnetotelluric studies suggest that the fault plane is rather impermeable since it separates differently resistive domains at different depth levels

[*Ritter et al.*, 2001].

The size of the damage zone is determined by a competition between localization and delocalization processes. The former are related to the brittle instability of damagable media [*Lyakhovsky et al.*, 1997], where as the latter may be related to the long term dynamics of the fault zone [*Lyakhovsky et al.*, 2001]. During the organization of a system of faults to form a planar fault zone, some fault strands dominate and take over the slip at the expense of other sub-parallel strands. If the rate of healing of distributed damage is high compared to the loading rate, the organization is slow. Furthermore, if healing saturates over the period of a seismic cycle, the seismicity is clustered, and no characteristic earthquake develops. Geologic studies of the DST indeed suggest ongoing organization [*Rotstein et al.*, 1992]. The historical seismicity is clustered as apparent from the quiescence since 1458, the year of a fourth earthquake in four centuries. Paleoseismic studies indicate further clustering of activity over periods of thousands [*Marco and Agnon*, 2003] to tens of thousands years [*Marco et al.*, 1996; *Amit et al.*, 2002]. High resolution archaeoseismic reconstruction of two historical devastating earthquakes show strong variability of slip, at odds with the characteristic earthquake model [*Ellenblum et al.*, 1998]. By contrast, the SAF shows characteristic earthquake behaviour [*Sieh and Jahns*, 1984] that is consistent with low healing to loading ratio. The SAF zone does not heal completely on the time scale of the seismic cycle, and ruptures tend to repeat on the same smooth trend [*Wesnousky*, 1994; *Stirling et al.*, 1996]. The AF seems to heal over the longer seismic cycle, so the trace is not as smooth. It remains to be seen whether the narrow gouge zone indicated here is a relic of the last earthquake, a product of ongoing creep, or a precursor of the next one.

The apparent narrowness of the damage zone gives evidence that the deformation along this large strike-slip fault is confined to a narrow region. This is further evidenced by conventional seismic experiments. These studies revealed a blocked velocity structure beneath the study area showing the AF separating a western low-velocity block and an eastern high-velocity block by rather large horizontal gradients, and showed indications for reflections from sub-vertical structures [*Maercklin et al.*, 2000]. The localized deformation along the DST as imaged by this study could support the supposition that the DST has originated in (and is cutting through) a relatively cold and stable continental lithosphere as proposed for example by *DESERT Team* [2002].

We revealed a waveguide along a 4 km segment of the AF. We were not successful in observing guided waves at larger offsets and for 9 other shots fired within the assumed fault trace. After all, this is not surprising when keeping in mind the narrowness of the waveguide and the given accuracy of *a priori* information on the fault trace. Furthermore, low-Q in the narrow waveguide attenuates the high-frequency waves quickly. However, this fact and the slight differences between the observations on line 4 and 5 suggest a variable structure (position of waveguides, continuity, etc.) along the studied AF segment.

8. Conclusions

With a specifically designed active seismic experiment in the Arava Valley, Jordan, we were able to record wave trains which were trapped in a sub-vertical, low-velocity waveguide. The locations of sources generating and receivers observing theses waves correspond to the surface trace of the Arava Fault, implying that this waveguide is the

damage zone of this prominent fault.

The modelling of the guided waves with a 2D analytical solution in conjunction with the systematic GA search for the best models (including proper evaluation) proved to be successful in obtaining important geometrical and petrophysical parameters of the AF. We derived a rather narrow shallow waveguide width of between 3 and 12 m. Although less constrained, the reduction of the waveguide velocity relative to the host rock velocity is in the range of between 10 and 60%.

The velocity reduction within the waveguide could be caused by damaged rock material and saturation with fluids which characterize the wear zone of this fault accumulated over time. According to scaling laws, the apparent narrowness of the damage zone (close to the surface) points toward a total slip of several hundreds of meters to several tens of kilometres along the AF fault at the shallow depth scale. Regarding the total DST slip of about 100 km, this can be understood considering a possible distribution of the slip on several faults in time and space (Quaira and Zofar faults etc.). Furthermore, rocks close to the surface east and west of the AF might have been formed syn-kinematically and, as a result, experienced less relative slip.

The very narrow low-velocity structure revealed by this study could not be detected directly by other seismic experiments carried out in the same area (reflection and refraction). In order to derive some of the parameters in similar experiments with high accuracy, we suggest to use a large number of sources and receivers (in-fault, cross-fault) and to use a broad frequency range (e.g., high sample rate).

Appendix A: Objective function

Our fitness function $F_{\hat{p}}$, which we maximize in the inversion, is calculated from a weighted mean of individual semblance values $s_{\hat{p},i}$ [*Neidell and Taner*, 1971] of each observed and synthetic trace pair i (M is number of traces) for a given set of model describing parameters $\hat{p} = (p_1, ...p_N)$ (N is number of parameters):

$$F_{\hat{p}} = \sum_{i=1}^{M} w_i s_{\hat{p},i}. \tag{A1}$$

Individual semblances $s_{\hat{p},i}$ are calculated from all samples k within the time window of interest of observed and synthetic traces (a_i and $b_{\hat{p},i}$, respectively) of trace pair i:

$$s_{\hat{p},i} = \frac{\sum\limits_{k}(a_{i,k} + b_{i,\hat{p},k})^2}{2\sum\limits_{k}((a_{i,k})^2 + (b_{i,\hat{p},k})^2)}. \tag{A2}$$

Semblance is 1 if traces are correlated, 0.5 if uncorrelated, and 0 if anti-correlated. The weight w_i increases the influence of traces with high signal energy in the inversion:

$$w_i = \frac{\sum\limits_{k}(a_{i,k})^2}{\sum\limits_{j=1}^{M}\sum\limits_{k}(a_{j,k})^2}. \tag{A3}$$

In order to accomplish small deviations of the true 3D subsurface structure from the simple 2D models we allowed time shifts of $\pm$ 1 sample ($\pm$ 2 sample for data of line 5/shot 101) between neighboring synthetic traces. Before calculating the objective function, we applied a uniform trace scale according to the maximal signal amplitude in the corresponding shot gather. Calculations were also conducted for reversed sign of the synthetic amplitudes.

Appendix B: Genetic Algorithm

Developed by John H. Holland, [e.g. *Holland*, 1975], genetic algorithms (GAs) search a multimodal parameter space for (global) maxima by using mechanics of natural selection and natural genetics [*Goldberg*, 1989]. Model describing parameters of a particular problem are first coded into binary strings. In a standard GA, a population of binary strings (that is a randomly chosen set of models) is modified by three operators, namely reproduction (selection), crossover and mutation. In the reproduction step individual strings are copied to the next generation according to their objective function values in a sense that higher values have higher probabilities to be copied. In the next step, offsprings are created from this mating pool by assembling substrings of parent binary strings. Substrings can be cut at one or more crossover positions. Finally, random mutations of single bits are performed on the population with a chosen (low) probability. This procedure is applied through many generations yielding a broad sampling of the parameter set while revealing one or more maxima. Since the invention of GA, modifications of and additions to this principal GA outline formed powerful search algorithms [e.g. *Goldberg*, 1989]. We used a population size of 50, mutation probability of 0.02, a (uniform) crossover probability of 0.5, and a creep mutation probability of 0.01. For in-depth discussion of GA and the settings please refer to *Goldberg* [1989] and *Carroll* [1996].

Acknowledgments.

For this analysis we used data of the Controlled Source Array (CSA) experiment as part of the Dead Sea Research Project (DESERT, http://www.gfz-potsdam.de/pb2/pb22/projects/deadsea/ds-home.html). DESERT was financed by the Deutsche Forschungsgemeinschaft (DFG), the GeoForschungsZentrum Potsdam (GFZ) and the Minerva Foundation. The Natural Resources Authority, Jordan, provided substantial logistical support. We thank K. Abu-Ayyash for his efforts. Furthermore we thank the Site Group (Jordan) and Chemical & Mining (Jordan) for their efforts with drilling and explosives. We grateful acknowledge the work of all field groups, in particular R. Ribhy, K.H. Jaeckel, S. Grunewald and G. Haim. Thanks to J. Mechie for supervising part of the drilling activities, and J. Bribach for technical assistance. Thanks to Yossi Bartov for fruitful discussions on the geology around the studied DST segment. We are indebted to the Associate Editor and reviewers Yehuda Ben-Zion and John Vidale for their critical remarks and helpful suggestions on the manuscript. We used instruments from the Geophysical Instrument Pool Potsdam (GFZ) and the FR Geophysics (Free University of Berlin). All figures were made using the generic mapping tool (GMT) [*Wessel and Smith*, 1995, 1998]. Thanks to David L. Carroll for making his GA code available. We took advantage of the CWP/SU seismic data processing packet [*Cohen and Stockwell Jr.*, 1999].

References

Abers, G. A., Hydrated subducted crust at 100-250 km depth, *Earth Planet. Sci. Lett.*, *176*, 323–330, 2000.

Aki, K., and P. G. Richards, *Quantitative Seismology*, W.H. Freeman and Co., USA, 1980.

Ambraseys, N., C. Melville, and R. Adams, *The Seismicity of Egypt, Arabia and the Red Sea*, Cambridge University Press, Cambridge, 1994.

Amit, R., E. Zilberman, Y. Enzel, et al., Paleoseismic evidence for time dependency of seismic response on a fault system in the southern Arava Valley, Dead Sea rift, Israel, *Geol. Soc. Am. Bull.*, *114*, 192–206, 2002.

Atallah, M., Tectonic evolution of the northern Wadi Arava, Jordan, *Tectonophysics*, *204*, 17–26, 1992.

Ben-Zion, Y., Properties of seismic fault zone waves and their utility for imaging low velocity structures, *J. Geophys. Res.*, *103*, 12,567–12,585, 1998.

Ben-Zion, Y., and K. Aki, Seismic radiation from an SH line source in a laterally heterogeneous planar fault zone, *Bull. Seismol. Soc. Am.*, *80*, 971–994, 1990.

Ben-Zion, Y., Z. Peng, D. Okaya, L. Seeber, J. G. Armbruster, N. Ozer, A. J. Michael, S. Baris, and M. Aktar, A shallow fault zone structure illuminated by trapped waves in the Karadere-Duzca branch of the North Anatolian Fault, western Turkey, *Geophys. J. Int.*, 2002, submitted.

Carroll, D. L., Chemical laser modeling with genetic algorithm, *American Institute of Aeronautics and Astronautics Journal*, *34*, 338–346, 1996.

Chester, F. M., J. P. Evans, and R. L. Biegel, Internal structure and weakening mechanisms of the San Andreas Fault, *J. Geophys. Res.*, *98*, 771–786, 1993.

Chon, Y.-T., W. Turpening, S. Rutherford, and M. Parchman, Reservoir continuity logging using connectivity mapping while drilling, *The Leading Edge*, *March*, 203–208, 1996.

Cohen, J. K., and J. W. Stockwell Jr., *CWP/SU: Seismic Unix Release 33: a free package for seismic research and processing*, Center for Wave Phenomena, Colorado School of Mines, 1999.

DESERT Team, Multinational geoscientific effort kicks off in the Middle East, *EOS Trans. AGU*, *81*, 609, 616–617, 2000.

DESERT Team, Structure and dynamics of the Dead Sea Transform, *Geology*, 2002, submitted.

Dresen, L., and H. Rüter, *Seismic Coal Exploration Part B: In-Seam Seismics*, Elsevier Scientific Publishing Company, New York, 1994.

Ellenblum, R., S. Marco, A. Agnon, T. Rockwell, and A. Boas, Crusader castle torn apart by earthquake at dawn, *Geology*, *26*, 303–306, 1998.

Eyal, M., Y. Eyal, Y. Bartov, and G. Steinitz, The tectonic development of the western margin of the Gulf of Elat Aqaba rift, *Tectonophysics*, *79*, 28 – 55, 1981.

Fukao, Y., S. Hori, and M. Ukawa, A seismological constraint on the depth of basalt-eclogite transition in a subducting oceanic crust, *Nature*, *303*, 413–415, 1983.

Garfunkel, Z., I. Zak, and R. Freund, Active faulting in the Dead Sea Rift, *Tectonophysics*, *80*, 1–26, 1981.

Gettemy, G., H. Tobin, J. Hole, and A. Sayed, Toward explaining scale-dependent velocity structure across an exposed brittle fault zone, *EOS Trans. AGU*, *82*, S41A–0583, 2001.

Gibson, S., and P. Charbonneau, Empirical modeling of the solar corona using genetic algorithms, *J. Geophys. Res.*, *103*, 14,511–14,521, 1998.

Goldberg, D. E., *Genetic algorithms in search, optimization, and machine learning,* Addison Wesley, Boston, 1989.

Holland, J., *Adaption in natural and artificial systems,* Ann Arbor: The University of Michigan Press, 1975.

Hough, S. E., Y. Ben-Zion, and P. C. Leary, Fault-zone waves observed at the southern Joshua Tree earthquake rupture zone, *Bull. Seismol. Soc. Am.*, *84*, 761–767, 1994.

Huang, B.-S., T. Teng, and Y. T. Yeh, Numerical modeling of fault-zone trapped waves: Acoustic case, *Bull. Seismol. Soc. Am.*, *85*, 1711–1717, 1995.

Igel, H., Y. Ben-Zion, and P. C. Leary, Simulation of $SH-$ and $P-SV-$wave propagation in fault zones, *Geophys. J. Int.*, *128*, 533–546, 1997.

Igel, H., G. Jahnke, and Z. Ben-Zion, Numerical simulation of fault zone guided waves: accuracy and 3-D effects, *Pure and Applied Geophysics*, 2001, in press.

Jahnke, G., H. Igel, and Z. Ben-Zion, Three-dimensional calculations of seismic fault zone waves in modestly irregular structures, *Geophys. J. Int.*, 2002, accepted.

Ken-Tor, R., A. Agnon, Y. Enzel, M. Stein, S. Marco, and J. F. Negendank, High-resolution geological record of historic earthquakes in the Dead Sea basin, *J. Geophys. Res.*, *106*, 2221–2234, 2001.

Klinger, Y., J. Avouac, L. Dorbath, N. A. Karaki, and N. Tisnerat, Seismic behaviour of the Dead Sea fault along Araba valley, Jordan, *Geophys. J. Int.*, *142*, 769–782, 2000.

Levin, V., and J. Park, P-SH conversions in a flat-layered medium with anisotropy of arbitrary orientation, *Geophys. J. Int.*, *131*, 253–266, 1997.

Li, Y.-G., and P. C. Leary, Fault zone trapped waves, *Bull. Seismol. Soc. Am.*, *80*, 1245–1271, 1990.

Li, Y.-G., and F. Vernon, Characterization of the San Jacinto fault zone near Anza, California, by fault zone trapped waves, *J. Geophys. Res.*, *106*, 999–999, 2001.

Li, Y.-G., and J. E. Vidale, Low-velocity fault-zone guided waves: Numerical investigations of trapping efficiency, *Bull. Seismol. Soc. Am.*, *86*, 371–378, 1996.

Li, Y.-G., P. Leary, K. Aki, and P. Malin, Seismic trapped modes in the Oroville and San Andreas fault zones, *Science*, *249*, 763–766, 1990.

Li, Y.-G., K. Aki, D. Adams, A. Hasemi, and W. H. Lee, Seismic guided waves trapped in the fault zone of the Landers, California, earthquake of 1992, *J. Geophys. Res.*, *99*, 11,705–11,722, 1994.

Li, Y.-G., K. Aki, and F. Vernon, San Jacinto fault zone guided waves: A discrimination for recently active fault strands near Anza, California, *J. Geophys. Res.*, *102*, 11,689–11,701, 1997a.

Li, Y.-G., W. L. Ellsworth, C. H. Thurber, P. E. Malin, and K. Aki, Fault-zone guided waves from explosions in the San Andreas fault at Parkfield and Cienega Valley, California, *Bull. Seismol. Soc. Am.*, *87*, 210–221, 1997b.

Li, Y.-G., K. Aki, J. E. Vidale, and M. G. Alvarez, A delineation of the Nojima fault ruptured in the M7.2 Kobe, Japan, earthquake of 1995 using fault zone trapped waves, *J. Geophys. Res.*, *103*, 7247–7263, 1998.

Li, Y.-G., K. Aki, J. E. Vidale, and F. Xu, Shallow structure of the Landers fault zone from explosion-generated trapped waves, *J. Geophys. Res.*, *104*, 20,257–20,275, 1999.

Li, Y.-G., J. E. Vidale, S. M. Day, F. Xu, E. Cochran, and D. Oglesby, Characterization of rupture zone of the Hector Mine and Landers, California, earthquakes using fault-zone guided waves, *EOS Trans. AGU*, *81*, F858–F859, 2000.

Lomax, A., and R. Snieder, The contrast in upper mantle shear-wave velocity between the East European Platform and tectonic Europe obtained with genetic algorithm inversion of Rayleigh-wave group dispersion, *Geophys. J. Int.*, *123*, 169–182, 1995.

Lou, M., J. A. Rial, and P. E. Malin, Modeling fault-zone guided waves of microearthquakes in a geothermal reservoir, *Geophysics*, *62*, 1278–1284, 1997.

Lyakhovsky, V., Y. Ben-Zion, and A. Agnon, Distributed damage, faulting, and friction, *J. Geophys. Res.*, *102*, 27,635–27,649, 1997.

Lyakhovsky, V., Y. Ben-Zion, and A. Agnon, Earthquake cycle, fault zones, and seismicity patterns in a rheologically layered lithosphere, *J. Geophys. Res.*, *106*, 4103–4120, 2001.

Maercklin, N., R. El-Kelani, C. Haberland, T. Ryberg, F. Scherbaum, M. Weber, and DESERT 2000 Group, DESERT 2000 - CSA: Seismic studies of the Arava fault, Dead Sea Rift Transform, Jordan, *EOS Trans. AGU*, *81*, F1203, 2000.

Malin, P. E., M. Lou, and J. A. Rial, *Fr* waves: A second fault-guided mode with implications for fault property studies, *Geophys. Res. Lett.*, *23*, 3547–3550, 1996.

Marco, S., and A. Agnon, Repeated earthquake faulting revealed by high-resolution stratigraphy, *Tectonophysics*, p. in press, 2003.

Marco, S., M. Stein, A. Agnon, and H. Ron, Long-term earthquake clustering: A 50,000-year paleoseismic record in the Dead Sea Graben, *J. Geophys. Res.*, *101*, 6179–6191, 1996.

Michael, A. J., and Y. Ben-Zion, Challenges in inverting fault zone trapped waves to determine structural properties, *Journal of Conference Abstracts*, *3*, 3547–3550, 1998a, conference on Mathematical Geophysics, July 12-17, 1998.

Michael, A. J., and Y. Ben-Zion, Inverting fault zone trapped waves with genetic algorithms, *EOS Trans. AGU*, *79*, S11C–16, 1998b.

Neidell, N., and M. T. Taner, Semblance and other coherency measures for multichannel data, *Geophysics*, *36*, 482–497, 1971.

Peng, Z., Y. Ben-Zion, and A. Michael, Quantitative inversion of seismic fault zone waveforms in the rupture zone of the 1992 Landers earthquake for structural properties at depth, *EOS Trans. AGU*, *82*, S32E–09, 2000.

Rabb'a, I., The Geology of the Al Qurayqira (Jabal Hamra Faddan), Map Sheet No. 3051 II), in *1:50.000 Geological Mapping Series*, Geological Bulletin No. 28, The Hashemite Kingdom of Jordan, Ministry of Energy and Mineral Resources, Natural Resources Authority, Geology Directorate, Geological Mapping Division, Amman, 1994.

Ritter, O., J. Schmidt, U. Weckmann, H. Thoss, A. Abueladas, and V. Haak, A 3D magnetotelluric study of the Dead Sea Transform fault in Jordan, *EOS Trans. AGU*, *82*, S41A–0582, 2001.

Rotstein, Y., Y. Bartov, and U. Frieslander, Evidence for local shifting of the main fault and changes in the structural setting, Kinarot basin, Dead-Sea transform, *Geology*, *20*, 251–254, 1992.

Rovelli, A., A. Caserta, F. Marra, and V. Ruggiero, Can seismic waves be trapped inside an inactive fault zone? The case study of Nocera Umbra, central Italy, *Bull. Seismol. Soc. Am.*, 2002, accepted.

Salamon, A., A. Hofstetter, Z. Garfunkel, and H. Ron, Seismicity of the eastern mediteranean region: Perspective from the Sinai subplate, *Tectonophysics*, *263*, 293–305, 1996.

Sambridge, M., and G. Drijkoningen, Genetic algorithm in seismic waveform inversion, *Geophys. J. Int.*, *109*, 323–342, 1992.

Scholz, C. H., Wear and gauge formation in brittle faulting, *Geology*, *15*, 493–495, 1987.

Schulz, S. E., and J. P. Evans, Mesoscopic structure of the Punchbowl Fault, Southern California

and the geologic and geophysical structure of active strike-slip faults, *Journal of Structural Geology*, *22*, 913–930, 2000.

Sen, M. K., and P. L. Stoffa, Rapid sampling of model space using genetic algorithms: examples from seismic waveform inversion, *Geophys. J. Int.*, *108*, 281–292, 1992.

Sieh, K. E., and R. H. Jahns, Holocene activity of the San Andreas Fault at Wallace Creek, California, *Geol. Soc. Am. Bull.*, *95*, 883–896, 1984.

Stirling, M. W., S. G. Wesnousky, and K. Shimazaki, Fault trace complexity, cumulative slip, and the shape of the magnitude-frequency distribution for strike-slip faults: A global survey, *Geophys. J. Int.*, *124*, 833–868, 1996.

Vidale, J., D. V. Helmberger, and R. W. Clayton, Finite-difference seismograms for sh waves, *Bull. Seismol. Soc. Am.*, *75*, 1765–1782, 1985.

Wallace, R., and H. Morris, Characteristics of faults and shear zones as seen in deep mines, *Pure and Applied Geophysics*, *124*, 107–126, 1986.

Wesnousky, S. G., The Gutenberg-Richter or characteristic earthquake distribution, which is it, *Bull. Seismol. Soc. Am.*, *84*, 1940–1959, 1994.

Wessel, P., and W. Smith, New version of the Generic Mapping Tools released, *Eos Trans. AGU*, *76*, 329, 1995.

Wessel, P., and W. Smith, New, improved version of the Generic Mapping Tools released, *Eos Trans. AGU*, *79*, 579, 1998.

Ch. Haberland, N. Maercklin, G. Rümpker, T. Ryberg, M. Weber, GeoForschungsZentrum Potsdam, Telegrafenberg E254, 14473 Potsdam, Germany, haber@gfz-potsdam.de,

nils@gfz-potsdam.de, rumpker@gfz-potsdam.de, trond@gfz-potsdam.de, mhw@gfz-potsdam.de

A. Agnon, Institute of Earth Sciences, The Hebrew University, Jerusalem 91904, Israel, amotz@cc.huji.ac.il

R. El-Kelani, An-Najah National University, Earth Sciences & Seismic Engineering Centre, P.O.Box 707, Nablus, Palestine Territories, radwan@najah.edu

I. Qabbani, Natural Resources Authority, P.O. Box 7, 11118 Amman, Jordan

F. Scherbaum, Institute of Geosciences, University Potsdam, PO 601553, 14415 Potsdam, Germany, fs@geo.uni-potsdam.de

Received -; revised -; accepted -.

To appear in the Journal of Geophysical Research

This manuscript was prepared with AGU's LaTeX macros v5, with the extension package 'AGU++' by P. W. Daly, version 1.6b from 1999/08/19.

Figure Captions

Figure 1. (left) Sketch showing the tectonic setting of the Middle East. (middle) Site map of the active seismic experiment at the Arava Fault (AF) as part of the Dead Sea Transform (DST). Fault trace (dark grey line) as inferred beneath superficial deposits. Shots are denoted by stars. Vertical sensors on lines 2 and 3 (spacing 100 m) are shown by triangles, 3-component sensors along lines 4 and 5 (spacing 10 m) are shown by squares. (right) Close-up of the region displayed in the middle panel. Filled symbols (stars, triangles, and squares as before) indicate shots generating and receivers observing guided waves, open symbols indicate shots and receivers without such generation or observation, respectively. Geology adopted from *Rabb'a* [1994] (NL: Na'ur limestone, LM: Neogene marl).

Figure 2. Observations on receiver line 4 (left) and line 5 (right) for the three shots 101 (top), 102 (middle), and 103 (bottom). For each gather, normalized maximum energy (bars, top, within time windows of 1.2 to 1.6 and 0.6 to 0.8 s, respectively), time series (middle) and spectra (bottom) for each trace are shown. Note the high-frequency wave trains from shots 101 and 102 on eastern traces of both lines between 1.3 and 1.6 s (line 4, left) and 0.6 and 0.8 s (line5, right), but no such phase for shot 103 (and all other shots; see text). For positions refer to Figure 1. Shown are unfiltered vertical component data containing presumed guided waves. P wave onsets (not shown) arrive at around 0.7 s (line 4, left) and 0.4 (line 5, right).

Figure 3. Waveforms calculated for synthetic model (for parameters refer to Table 3). We added random static shifts of at most $\pm$ 0.005 s and random noise (maximum signal-to-noise ratio of 5) to the synthetics. Shown are raw synthetics (thin line) and synthetics with noise (thick line) which we used in the recovery test.

Figure 4. A-D: Fit of all in the GA search tested models (synthetic recovery test) displayed for the 4 free parameters. Grey dots and black crosses indicate $F < 0.85$ and $F > 0.85$, respectively. The parameters of the synthetic input model together with its associated F value are denoted by black star. The dashed line marks the F level of the best model found. E: Cross-plot of all acceptable models (F colour coded; red denote high values, purple denote low fit values) as a function of w and $v_{s,2}/v_{s,1}$ illustrating the strong trade-off between these two parameters (synthetic recovery test). The synthetic input model is represented by the black star. Data were sorted according to F value prior to plotting. F: Cross-waveguide velocity distribution of acceptable models for the synthetic recovery test. Grey (black) lines represent models with $0.8 < F < 0.85$ ($F > 0.85$). The synthetic input model is represented by the red line.

Figure 5. Search results for shot 101 observed at line 4. Notations as in Figure 4 except that grey dots and black crosses indicate $F < 0.98 \cdot F_{best}$ and $F > 0.98 \cdot F_{best}$, respectively.

Figure 6. Search results for shot 102 observed at line 4. Notations as in Figure 4 except that grey dots and black crosses indicate $F < 0.98 \cdot F_{best}$ and $F > 0.98 \cdot F_{best}$, respectively.

Figure 7. Search results for shot 101 observed at line 5. Notations as in Figure 4 except that grey dots and black crosses indicate $F < 0.98 \cdot F_{best}$ and $F > 0.98 \cdot F_{best}$, respectively.

Figure 8. Cross-waveguide velocity distribution of acceptable models ($F > 0.73$) of the observations on line 4 (shots 101 and 102). Different shading indicates how often a particular model component was found in the searches (from light to dark increasing frequency). The distinct black vertical lines show that most well-fitting models are characterized by a 4 to 6 m wide waveguide.

Figure 9. Synthetics of the best models (thin line) and corresponding data (thick line) of shot 101 (top) and 102 (middle), line 4, and of shot 101 observed at line 5 (bottom). Observed traces have been shifted ($\pm$ 1 or 2 samples relative to the neighboring traces) according to the values derived in the inversion.

Tables

Table 1. Positions of shots generating guided waves

id	latitude ($^\circ N$)	longitude ($^\circ E$)	altitude (m)
s101	30.57800	35.33440	33.0
s102	30.57800	35.33311	21.7

Table 2. Positions of receiver line segments recording guided waves

id	latitude ($^\circ N$)	longitude ($^\circ E$)	altitude (m)
412	30.55746	35.32787	31.0
413	30.55745	35.32798	30.9
414	30.55743	35.32808	31.3
415	30.55742	35.32818	31.4
416	30.55741	35.32828	31.6
504	30.58718	35.33677	36.3
505	30.58724	35.33669	36.7
506	30.58730	35.33660	36.7
507	30.58734	35.33652	36.9
508	30.58738	35.33638	34.2
509	30.58742	35.33629	33.8
510	30.58747	35.33621	33.2

Table 3. Parameters used for synthetic test and search results

Parameter	value used in forward calculation	range of values revealed by the search	best value found in search
$v_{s,1}$ (m/s)	1750	1710 - 1775	1713
$v_{s,2}/v_{s,1}$	0.6	0.4 - 0.9	0.43
w (m)	5	3 - 18	3.31
Q_s^{-1}	0.005	0 - 0.013	0.011
ρ (kg/m^3)	2500	-	-
x_s	at interface	-	-

Table 4. Parameters derived by inversion of data recorded along line 4 and 5. For each parameter ranges and best values are given.

Parameter	shot 101/line 4		shot 102/line 4		shot 101/line 5	
	range	best value	range	best value	range	best value
$v_{s,1}$ (m/s)	1685 - 1870	1742	1694 - 1850	1847	1570 - 1780	1710
$v_{s,2}/v_{s,1}$	0.4 - 0.95	0.43	0.4 - 0.62	0.44	0.45 - 0.95	0.84
w (m)	3 - 35	3.70	4 - 7	4.47	2 - 27	6.02
Q_s^{-1}	0.005 - 0.025	0.013	0.005 - 0.015	0.006	0 - 0.015	0.0014

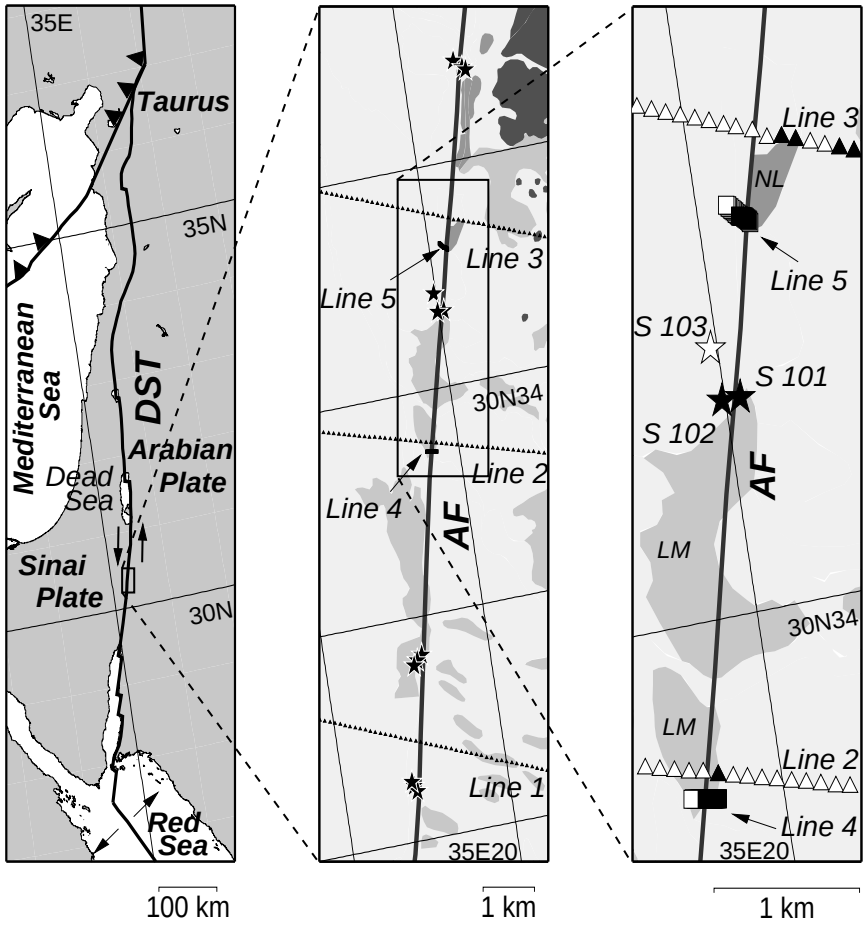
35E
Taurus
35N
Mediterranean Sea
DST
Arabian Plate
Dead Sea
Sinai Plate
30N
Red Sea
100 km
Line 3
Line 5
30N34
Line 2
Line 4
AF
Line 1
35E20
1 km
Line 3
NL
Line 5
S 103
S 101
S 102
AF
LM
30N34
LM
Line 2
Line 4
35E20
1 km

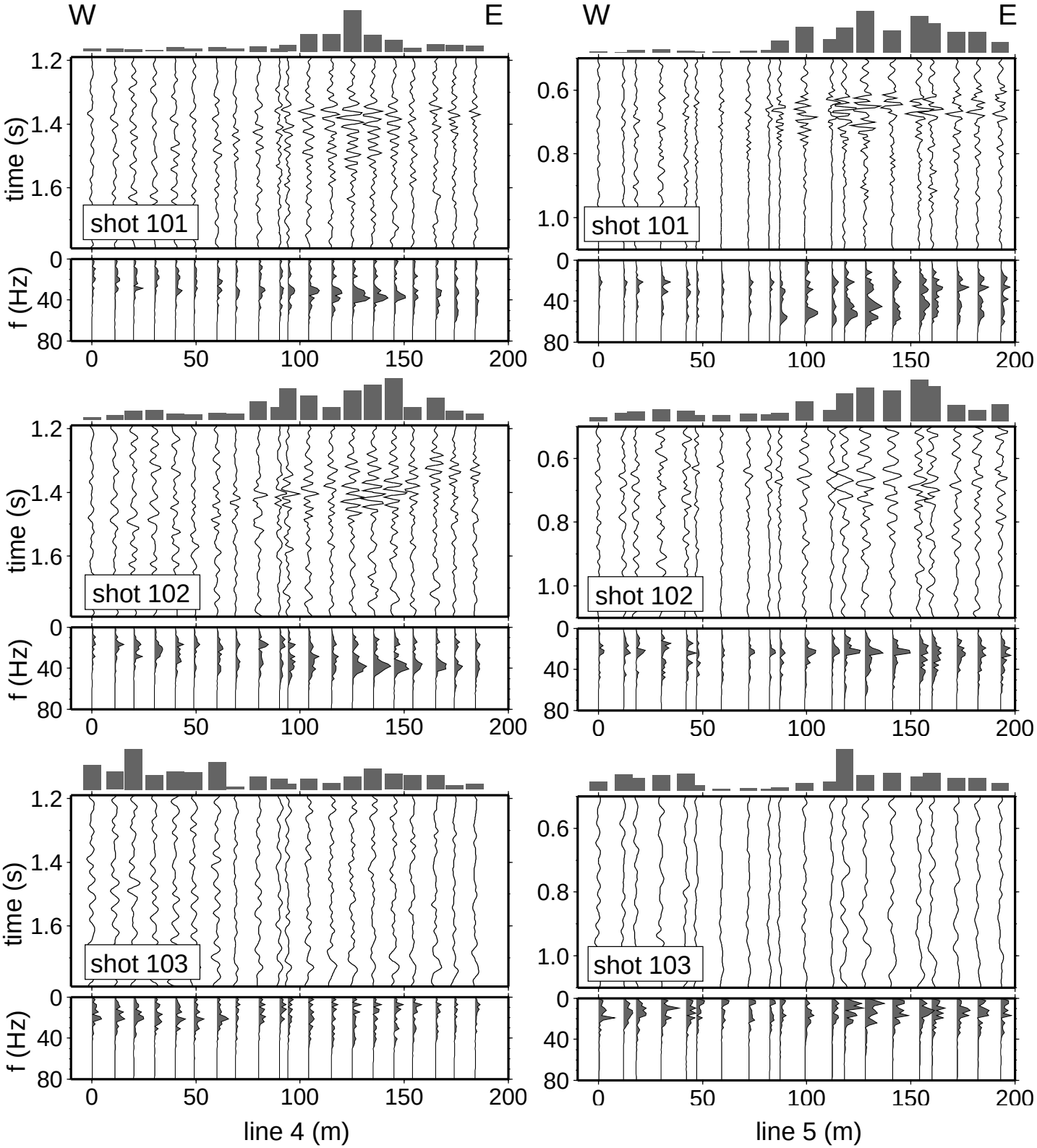

Fig. 2

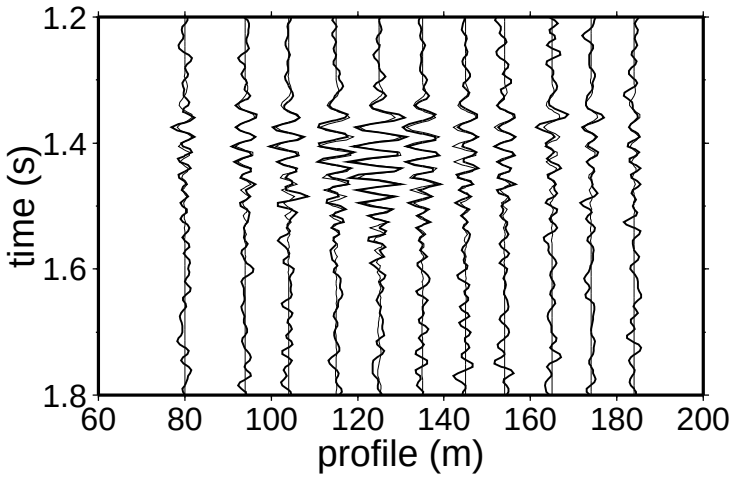

Fig. 3

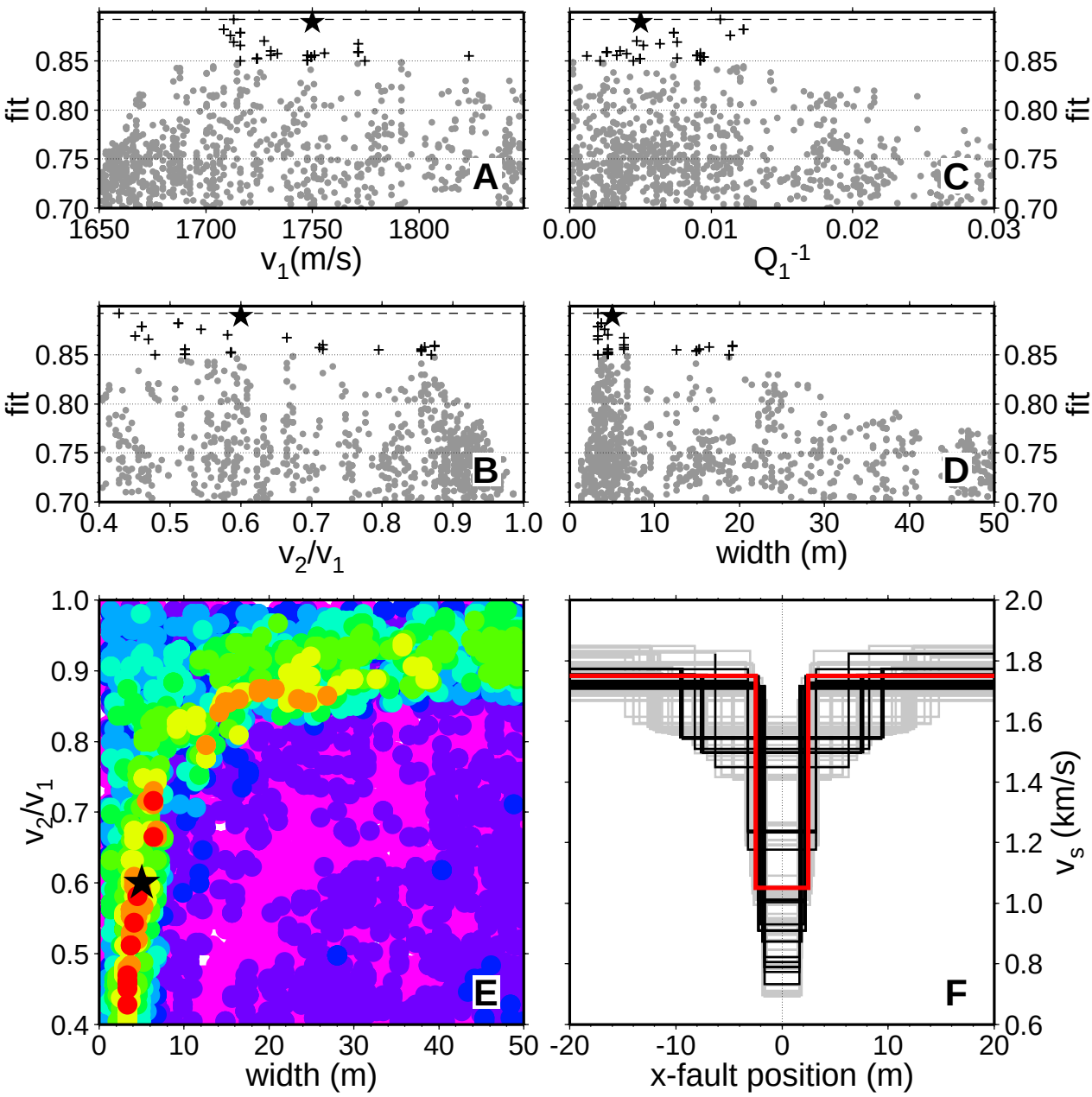
A
B
C
D
E
F
fit
0.85
0.80
0.75
0.70
1650
1700
1750
1800
v1(m/s)
0.00
0.01
0.02
0.03
Q1-1
0.4
0.5
0.6
0.7
0.8
0.9
1.0
v2/v1
0
10
20
30
40
50
width (m)
1.0
0.9
0.8
0.7
0.6
0.5
0.4
v2/v1
-20
-10
0
10
20
x-fault position (m)
2.0
1.8
1.6
1.4
1.2
1.0
0.8
0.6
vs (km/s)

Fig. 4

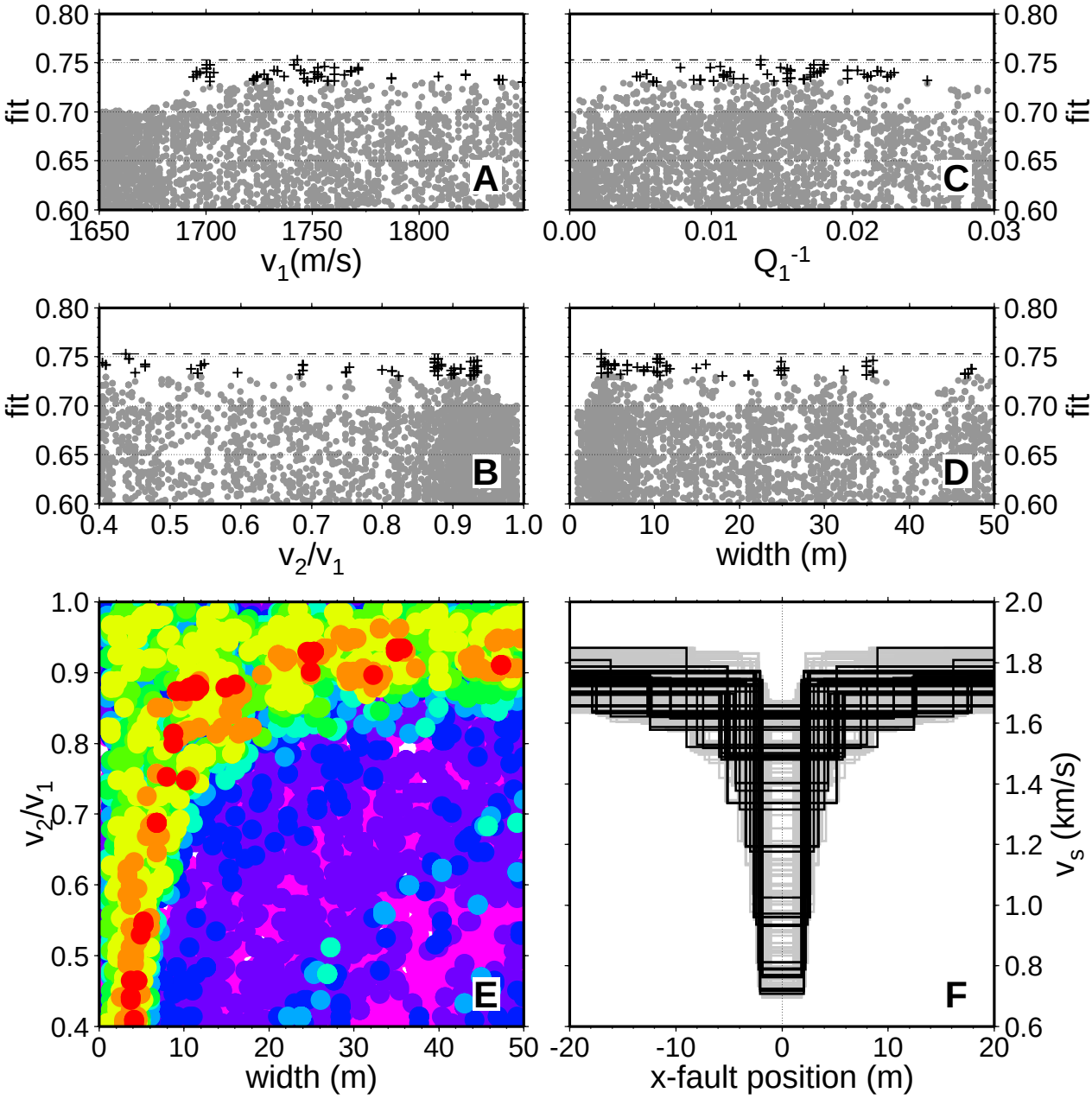

Fig. 5

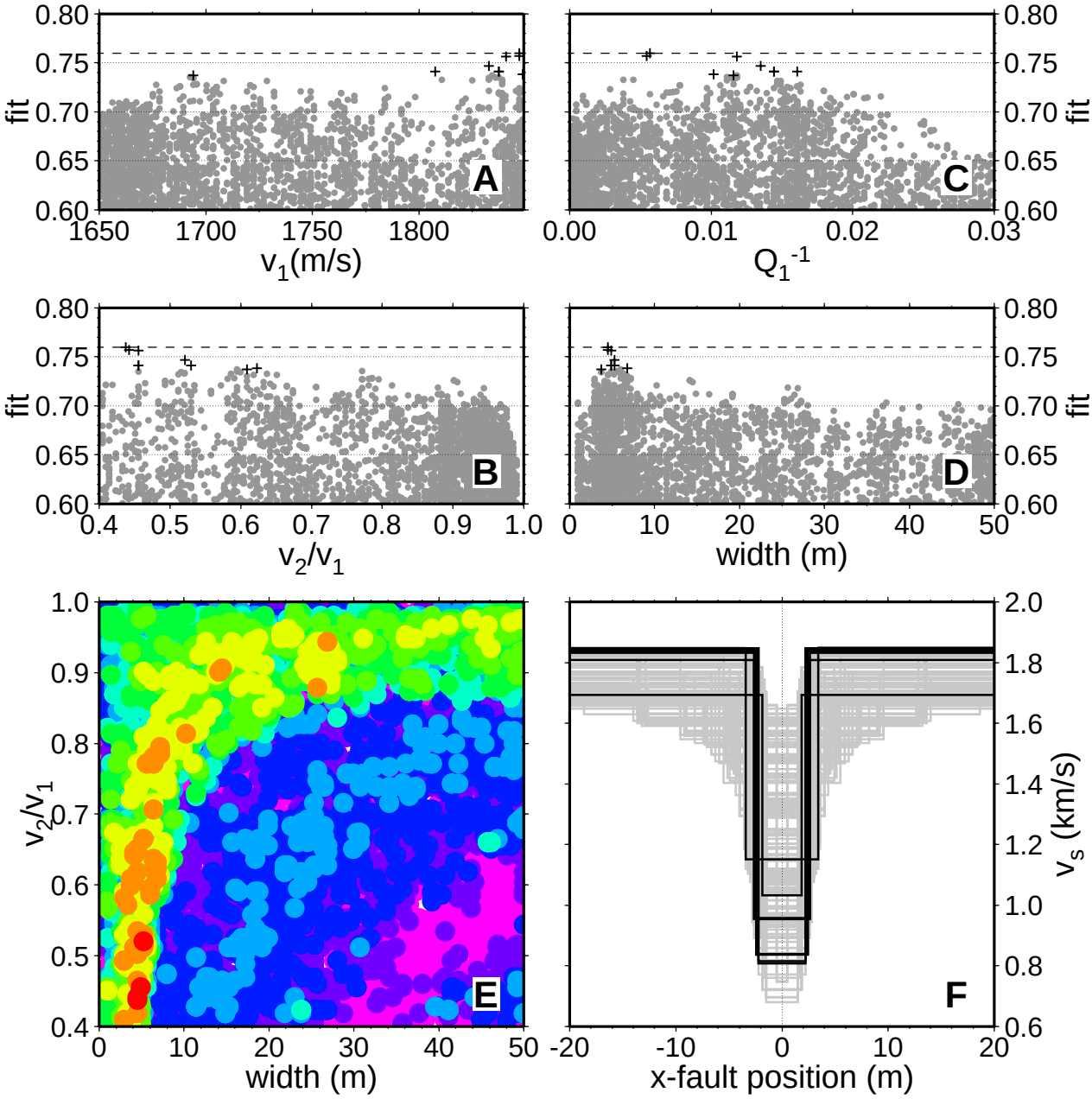

Fig. 6

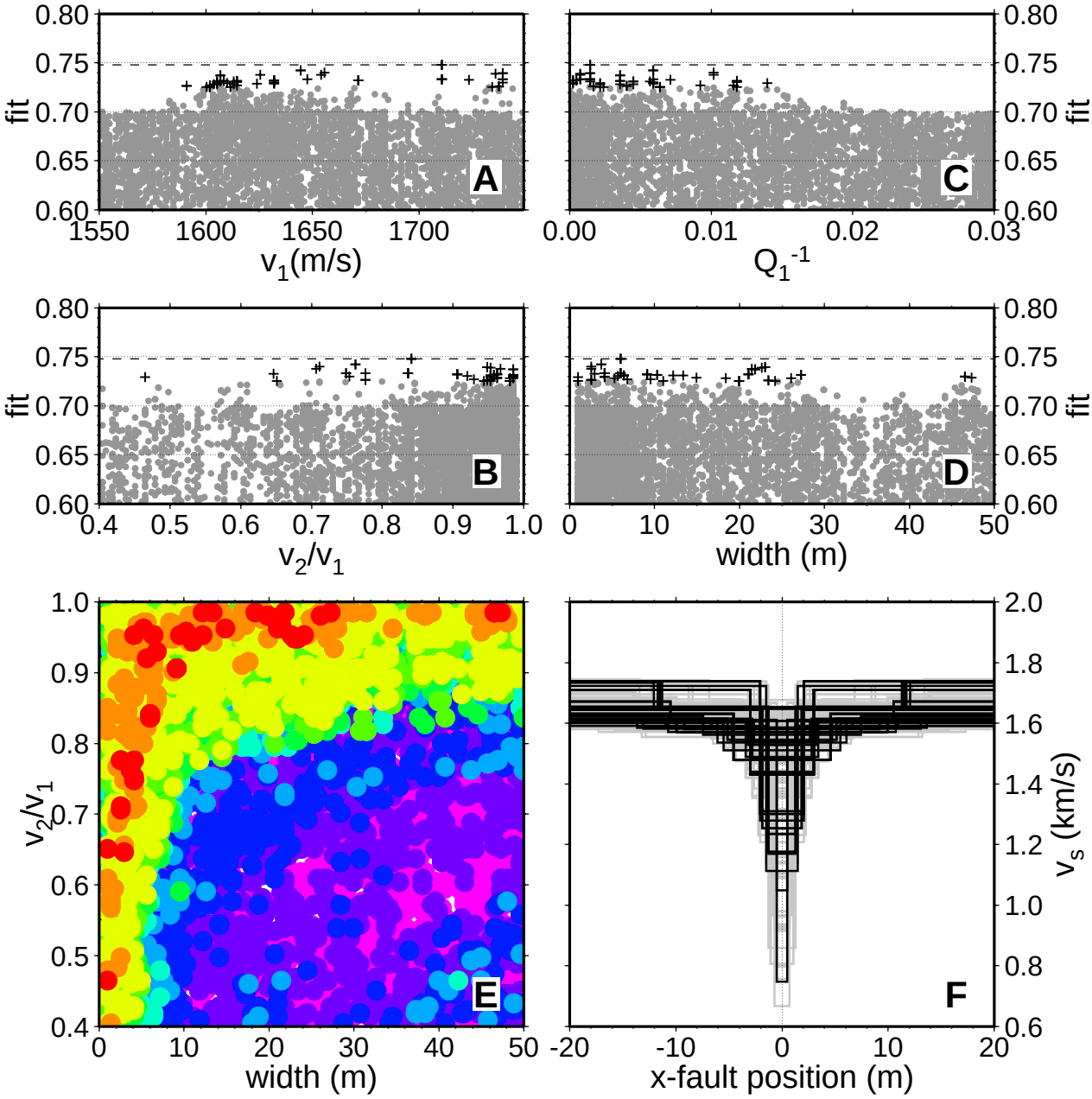

Fig. 7

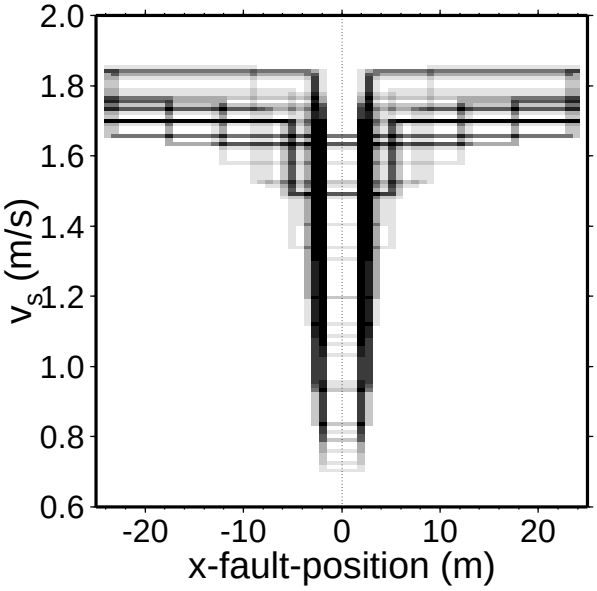

Fig. 8

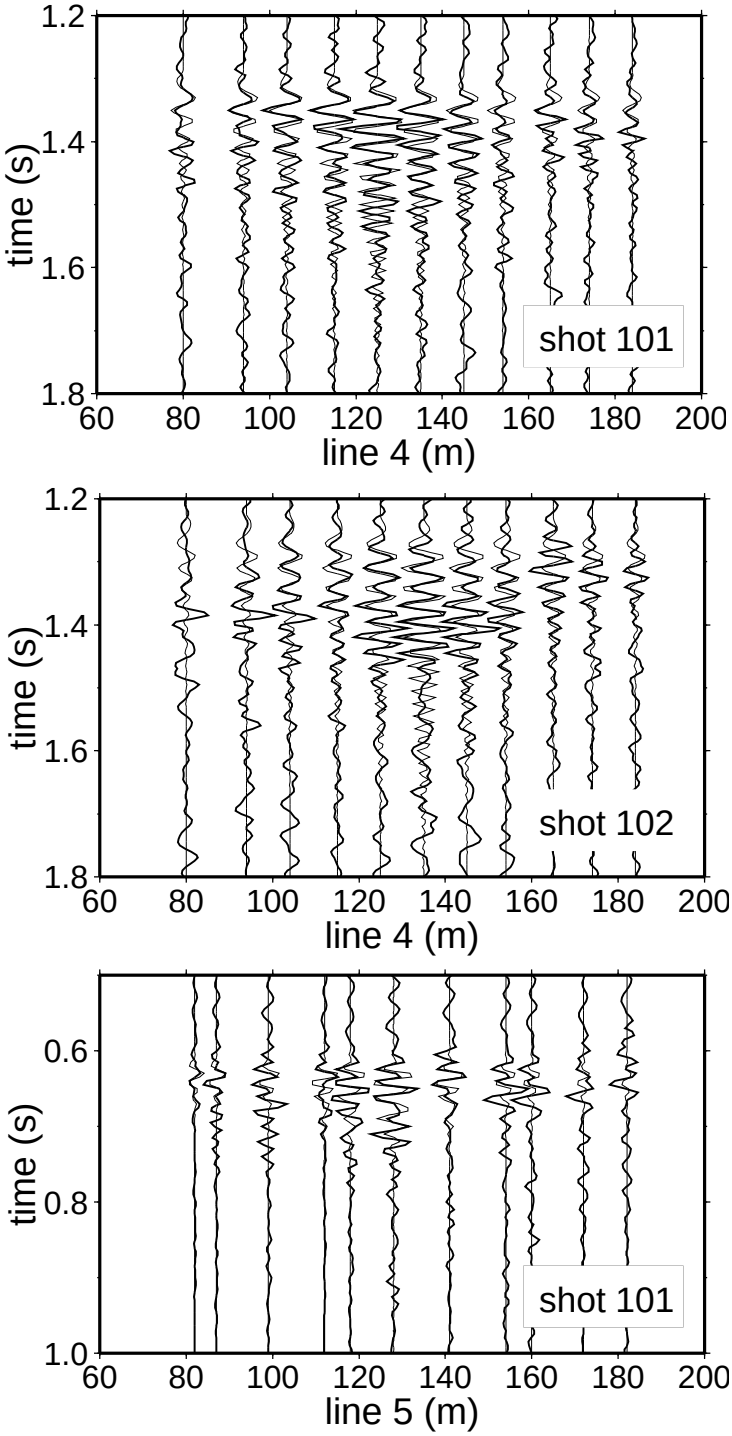
1.2
1.4
1.6
1.8
time (s)
shot 101
60
80
100
120
140
160
180
200
line 4 (m)
1.2
1.4
1.6
1.8
time (s)
shot 102
60
80
100
120
140
160
180
200
line 4 (m)
0.6
0.8
1.0
time (s)
shot 101
60
80
100
120
140
160
180
200
line 5 (m)

Fig. 9